ORIGINAL ARTICLE

A Clinical Planning Module for Adaptive Optics SLO Imaging

Gang Huang, Xiaofeng Qi*, Toco Y. P. Chui*, Zhangyi Zhong*, and Stephen A. Burns*

ABSTRACT

Purpose. To develop a clinical planning module (CPM) to improve the efficiency of imaging subjects with a steerable wide-field adaptive optics scanning laser ophthalmoscope (AOSLO) and to evaluate the performance of this module by imaging the retina in healthy and diseased eyes.

Methods. We developed a software-based CPM with two submodules: a navigation module and a montage acquisition module. The navigation module guides the AOSLO to image identified retinal regions from a clinical imaging platform using a matrix-based mapping between the two. The montage acquisition module systematically moves the AOSLO steering mirrors across the retina in predefined patterns. The CPM was calibrated using a model eye and tested on five normal subjects and one patient with a retinal nerve fiber layer defect.

Results. Within the central ±7° from the fixation target, the CPM can direct the AOSLO beam to the desired regions with localization errors of <0.3°. The navigation error increases with eccentricity, and larger errors (up to 0.8°) were evident for regions beyond 7°. The repeatability of CPM navigation was tested on the same locations from two subjects. The localization errors between trials on different days did not differ significantly (p > 0.05). The region with a size of approximately 13° × 10° can be imaged in about 30 min. An approximately 12° × 4.5° montage of the diseased region from a patient was imaged in 18 min.

Conclusions. We have implemented a clinical planning module to accurately guide the AOSLO imaging beam to desired locations and to quickly acquire high-resolution AOSLO montages. The approach is not only friendly for patients and clinicians but also convenient to relate the imaging data between different imaging platforms.
(Optom Vis Sci 2012;89:593–601)

Key Words: adaptive optics, scanning laser ophthalmoscope, retinal nerve fiber layer, clinical planning module

Adaptive optics scanning laser ophthalmoscope (AOSLO) allows real time imaging of cellular and subcellular structure in the living human eye. In recent years, AOSLO systems have been used for a growing range of scientific and clinical applications, including detailed measurements of the photoreceptors,[1–4] vasculature,[5–8] and other retinal structures.[9,10] However, adaptive optics (AO) imaging systems typically have a field of view (FOV) of only a few degrees due to optical limitations,[11] and this can lead to problems of targeting the high resolution imaging to specified regions of interest on the retina. A typical approach is to image a recognizable landmark first and then move the imaging region toward the target region by asking the subject to fixate different targets in spatial sequence, often using a movable fixation spot or a fixation array. If a montage of the affected retinal region is required, the patient is asked to sequentially fixate a series of neighboring fixation targets or a movable target. Burns and co-

workers[12] introduced a different approach by designing a steerable AOSLO combined with a wide-field line scanning ophthalmoscope. The steering angle in the most recent version is extended to almost 30° of the posterior pole without requiring refixation by the subject.[13] The wide-field imaging video can guide the high-resolution imaging session in real time. Both approaches are convenient for both the experimenter and the subject but can be difficult to relate to other clinical imaging modalities. For the Burns' approach,[12,13] this arises because the wide-field image quality was made subordinate to AOSLO image quality and thus identifying and navigating to specific clinical features can be difficult. Therefore, for both these currently used approaches for AOSLO imaging, there can be difficulties in relating the very high-resolution images to clinical images during the measurement session and thus be assured that the entire region of interest has been imaged.

For this reason, we developed a clinical planning module intended to relate regions of interest from a common clinical imaging system directly to the AOSLO steering system. This module would

*PhD
Indiana University, School of Optometry, Bloomington, Indiana.

allow the experimenter to guide the AOSLO directly to regions of interest using a fundus image available in clinics and then to rapidly acquire a montage of the region around that location without requiring refixation by the subject. The overall goal of this development was to simplify the imaging session for the patient and also to improve the efficiency and throughput of an AOSLO imaging session without sacrificing the high quality of AOSLO imaging that has been widely demonstrated. In the article, we present the techniques involved and provide initial data generated using this clinical planning module.

METHODS

The Indiana AOSLO

The wide-field AOSLO has been described previously.[13] In brief, two deformable mirrors (DM) are used to correct the ocular monochromatic aberrations in a closed-loop feedback system. Of these two DMs, one is a 52-actuator, 50 μm stroke DM (Imagine Eyes) for the correction of large-amplitude low-order aberrations and the other is a 140-actuator, 4 μm stroke DM (Boston Micromachines Corporation) which is used for high-order aberration correction. The imaging wavelength is 840 nm and the size of each AO image is 2.00° × 1.8°. The size of the confocal aperture in the system is approximately twice the size of the theoretical Airy disc. The optical resolution of the system is 2.4 μm for a 7 mm pupil, although the system works with any size pupil from 3 to 8 mm and has been shown to produce images meeting the expectations of a confocal system operating near the diffraction limit.[14] Videos are recorded at a frame rate of 30 Hz, using a maximum of 150 μW of 840 nm light (measured at the pupil plane). Light levels are safe according to the American National Standards Institute (ANSI) standards.

To achieve wide-field steering capability, the system incorporates a field mirror that subtends approximately 30° at the retina. The AOSLO imaging beam can be moved to any location within this field by adding offset voltages to the horizontal and/or vertical steering mirror. A fixation target is provided by either a LED mounted outside the 30° FOV or by a programmable video fixation system that is mapped within the wide FOV of the system.

Clinical Planning Module

The clinical planning module consists of two submodules. The first submodule is a navigation module which allows clinicians or operators to identify regions of interest on a clinical image by clicking on the central pixels of the clinical regions of interest. The field size of each clicked region is the same as the AOSLO's. Multiple regions (clicks) are typically necessary to cover both the normal and pathological regions. The locations of the regions as well as the clinical image are then used to control the AOSLO navigation module. This module guides the steerable AOSLO to the region of interest for high-resolution imaging by transforming the coordinates of those regions on the clinical image to the steering mirror's position. Because both the AOSLO and clinical fundus imaging platforms define the image pixel position as the visual angles subtended at the pupil plane of the eye,[15] the transformation is used to match the pixel angular position of one platform to the other. The

actual spatial position of the pixel on the retina is not involved in the transformation. In addition to angular size or scale differences between systems, it is also necessary to correct translation and rotations of the pixel position between the two imaging platforms. Therefore, a 2 × 2 transformation matrix was used, where the four coefficients of the matrix can model any combination of scale, rotation, and translation between the imaging coordinates of the AOSLO and the clinical fundus imaging platform.

In this study, a Spectralis OCT (Heidelberg Engineering, Heidelberg, Germany) was selected as the clinical fundus imaging platform and its confocal scanning laser ophthalmoscope (cSLO) infrared image was used as the clinical image. The cSLO infrared image from the Spectralis is referred as a cSLO image throughout the article. The mapping between the steerable AOSLO and the Spectralis was measured in a series of steps. First, we created a "model eye" with a 30° FOV. The model eye consists of an achromatic lens of 100 mm focus length in the pupil plane and a patterned paper target located 100 mm from the lens. By imaging the model eye under identical conditions on both instruments, we can be confident that a given location on the target of the model eye represented identical pixel angles for both systems. For the Spectralis, the entire region was imaged in a single cSLO image. The corresponding coordinates of the AOSLO steering mirror were then determined by steering the AOSLO image field such that the same features of the target were located in the center of the AOSLO video frame and recording the steering mirror positions. For a given location, its pixel position in the cSLO image and the corresponding position of the AOSLO steering mirror were defined as a corresponding point pair. The transformation matrix was then computed by least square fitting the coefficients of the matrix with five corresponding point pairs. During the matrix computation, one of the pairs was defined as the fovea pair for the model eye. The relative distance of the other four pairs to the fovea pair was then calculated and used to compute the four coefficients of the matrix. Typically, we select the center of the cSLO image and its corresponding AOSLO steering mirror position as the fovea pair for the model eye. With this matrix and the fovea pair, pixel positions on the cSLO image can be transformed to steering mirror positions of the AOSLO.

With the same model eye, three sets of transformation matrices were determined by different strategies for selecting corresponding point pairs, and the performance of the strategies were evaluated. To perform this evaluation, one hundred features were identified within a circular region with a radius of 10° centered on the "fovea" of the model eye's cSLO image such that there were 10 features within each 1° annular ring. Their positions in the two imaging platforms form 100 corresponding point pairs. The first strategy selected five pairs of points within the central ±2° circular region of the cSLO image. It was expected that high mapping precision would be achieved in the central region using this strategy, but the accuracy was expected to decrease with increased distance. The second strategy selected five uniformly distributed pairs within the central ±10° circular region to better model the global transformation as opposed to the foveal transformation. The third strategy divided the whole ±10° circular region of the cSLO image into five circular bands with a 2° separation, and then five features from each band were used to calculate the transformation matrix for that band, resulting in five transformation matrices. The aim of the

third approach was to test whether the global performance could be further optimized by adopting different matrices as opposed to the second strategy which only used a single matrix. Performance for each strategy was determined by first using the matrix to direct the AOSLO steering mirror to position the imaging field at the feature determined from the cSLO image and then computing the difference between a feature's actual location in the AOSLO frame and the center of the AOSLO frame in units of degrees. The difference was defined as the mapping error. For all three strategies, those corresponding point pairs not used to determine the matrix were used to evaluate the performance of the corresponding matrices. For the third strategy, the system would first determine which circular band the pair fell into and then use the appropriate matrix. For an error-free case, the selected feature would fall onto the center of the AOSLO image frame and the mapping error would be zero.

When the navigation module was applied to a subject, the same matrix determined from the model eye was used while the fovea pair used in the model eye required updating. The fixation target position in the AOSLO and the fovea pixel position of the cSLO image form a new fovea pair for the subject. An additional step of manual identification of the fovea was required before applying the navigation module to human subjects. This was required because the Spectralis cSLO did not have a sufficiently precise method for placing its fixation target and thus the fovea was not always located in the center of the cSLO field. We therefore first click on the approximate location of the fovea on the cSLO image and then calculated a transform matrix for that approximate foveal point pair. There could still be an error however arising from inaccurate identification of the fovea position on the cSLO image. The error causes an extra translation of the fovea pair and thus generates a new offset error. Therefore, after aligning the subject to the AOSLO, we identified a landmark near the fovea on the cSLO image such as a recognizable vessel crossing, and the AOSLO steering mirror moved the imaging field to the location calculated by the first estimate of the transform. The operator then made a fine adjustment of the AOSLO steering mirror to center the vessel crossing in the AOSLO image. The fovea pair was then updated automatically with this offset correction. If the experimenter intentionally moved the fixation target, for instance to image peripheral retina, then the procedure was repeated.

The second submodule is a montage acquisition module. This module allows the experimenter to predefine one or a series of montage sampling patterns for the AOSLO imaging and quickly sample the whole region. For a given imaging region, a montage pattern is defined by a series of locations in a text file. These locations represent the specified offset values relative to the starting location of the montage. To use the montage acquisition module, the AOSLO imaging field is first navigated to a region of interest using a mouse click on the cSLO image displayed in the navigation module, and then the montage acquisition module automatically moves the imaging field to each relative location in sequence. The module requires the operator to decide to either accept the image sequence at a location or to repeat the imaging at that location. This allows the operator to give the subject an opportunity to blink or to retake the image of a region if image quality is not acceptable. The montage pattern and sizes are easily generated by the operator. For example, for a small defect <1°, a sampling pattern of 3 × 3

raster sampling grid with 1° separation can be defined. For a large region of interest, a larger set of offsets would be used.

Data Acquisition

Six subjects participated in this study to evaluate the performance of the module. The right eyes of each subject were imaged. All subjects were dilated using 0.5% Tropicamide. No corrective lenses were worn during the study. Subject ages were between 25 and 65 years. Subjects 1 to 5 were healthy and had no ocular disease. Subject 6 was diagnosed with cotton wool spots and the retinal nerve fiber layer (RNFL) defects can be visualized on the subject's fundus image.[16] Research procedures were performed in accordance with the Declaration of Helsinki. The study protocol was approved by the institutional review boards of Indiana University, and all subjects provided written informed consent after explanation of the risks and benefits of the study were explained and before participation in the studies.

For subjects 2 and 3, the navigation module was evaluated by measuring the mapping errors of selected retinal features. At least 20 vasculature features on each subject's cSLO image were determined before the AOSLO imaging. Features were chosen within ±10° retinal eccentricity. During imaging, each feature was clicked and the AOSLO was guided by the navigation module to the calculated position. As soon as the subject's fixation stabilized, the video was acquired. After the testing session, the first acceptable quality frame in the video was selected as the reference frame. The distance between the center of the target feature in the reference frame and the center of the frame was measured as the mapping error for that feature. To test the repeatability of the method, both subjects were imaged twice, selecting the same features on different days.

To test the montage acquisition module, the operator systematically imaged the RNFL using a predefined region of approximately 13° × 10° for all normal subjects. Two extra regions of RNFL were imaged from subjects 4 and 5 to assess the feasibility of acquiring larger montage data within a single session. For subject 6 who has a RNFL defect, an approximately 12° × 4.5° region covering the affected region and nearby unaffected regions was imaged. To test whether operators could satisfactorily operate the system without simultaneous wide-field imaging, the line scanning ophthalmoscope[13] in the AOSLO was turned off. All data acquisition was completed using only the steerable AOSLO and offline cSLO images.

After the testing session, image frames were extracted from the video and processed offline to reduce the interframe and intraframe eye movement.[17] For each imaging location, multiple frames (typically 5 to 20 frames) were aligned and averaged to improve the signal to noise ratio. Multiple small field images were then stitched together to create a retinal montage using Adobe Photoshop CS4 (Adobe Systems, San Jose, CA).

Statistical Analysis

For the results obtained on the model eye, the probability of differences in performance for the three strategies arising by chance was computed using the Student's t-test (two tails, paired) in two approaches. In the first, the entire central ±10° circular region
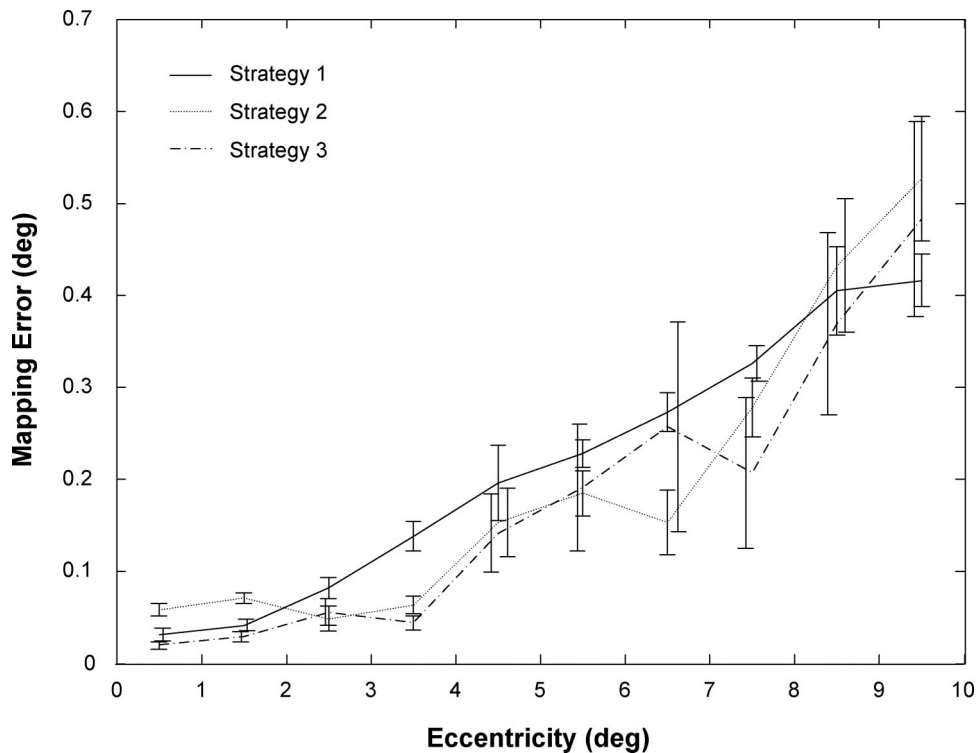
FIGURE 1.

Mapping error as a function of eccentricity on the model eye. Data represents average errors within 1° intervals from the fovea (the center of the cSLO image). Strategy 1 involved fitting only points within the central region. Strategy 2 fit data points further from the center of the field. Strategy 3 fit the transform within annuli (see text). Error bars represent standard errors and show that not only does the average error increase but there is variability in the error depending on the exact eccentricity.

with 75 pairs of mapping errors was compared. In the second, individual t-tests were run for binning data in 2° annular bins. For the second test, 15 pairs of mapping error were used for each t-test. For human eyes, the repeatability of the navigation module between trials was examined using a t-test (two tails, paired comparisons). Twenty features in each trial were used for the comparison. Where multiple tests were performed, a Bonferroni correction was applied to the significance level such that we considered a result as significant if it had <5% probability of occurring by chance.

RESULTS

The navigation module performed better at the center of the imaging systems than at higher eccentricities when the module was tested on the model eye with the transformation matrix computed by any of the three strategies (Fig. 1). The averaged errors were calculated by averaging the mapping error in 1° bins. The standard errors (SEs) of each averaged error were also computed. No significant difference was found between three strategies ($p > 0.05$). The averaged errors within the central ±2° circular region are <0.1°, approximately 6% of the frame size of the AOSLO. When the imaging field of the AOSLO was moved further from the center, the error increased, suggesting that the mapping relation between the two instruments changed with distance from the center of the field. However, between the central 2° to 6° region, the averaged errors of strategy 2 (0.12°; SE ±0.02°) and strategy 3 (0.10°; SE ±0.02°) are smaller than that of strategy 1 (0.18°; SE ±0.02°). Strategy 1 differed from strategies 2 and 3 ($p < 0.05$), but the latter

two strategies did not differ. This result suggests that strategies 2 and 3 have better global mapping capabilities than strategy 1, as we expected. We also looked at the maximum error of each strategy because the maximum error can limit practical use, and here the maximum errors over the central ±10° circular region were between 0.7° to 0.8°, which means that the feature selected in the cSLO image would appear at the margin of the AOSLO frame. However, for strategies 2 and 3, these large errors occurred only when the eccentricities were larger than approximately 7° and only for some locations within the field. To guarantee that selected features appear within the central region of the frame, the imaging region could be restricted to be within ±7° region where the maximum errors of both strategies were under 0.3°, approximately 20% of the frame size. As strategies 2 and 3 were not reliably different in their performance, and strategy 2 was simpler, the matrix computed with strategy two was used to test the human subjects.

The performance of the navigation module was similar when tested on human subjects to performance measured with the model eye. The displacement of features selected from the cSLO image from the center of the AOSLO image increased with increasing eccentricity. Within the central ±7° circular region, the feature selected by mouse clicking on the cSLO image was always within the central region of the AOSLO imaging field. Example images are shown in Fig. 2. The averaged error was computed by averaging the mapping error per trial for each subject for the desired region. Within this central ±7° circular region, the averaged error was less
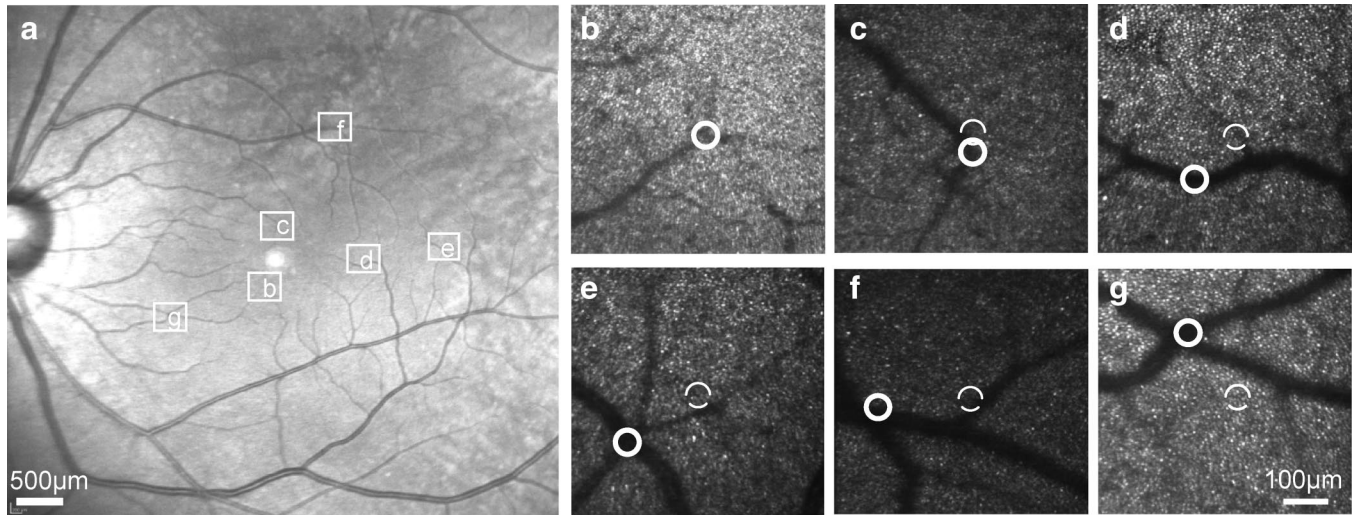
FIGURE 2.

An example of the navigation module performance from subject 3. (a) The cSLO mode image acquired from the Heidelberg Spectralis. The white squares in the image represent the locations where AOSLO images were requested via mouse click. (b–g) The actual AOSLO images acquired by clicking at the locations indicated by the white squares in (a). Ideally, the targeted feature from (a) would be at the center of the AOSLO frame. The solid circle in (b–g) show the feature and the dashed circles represent the frame centers. The error is the distance between these two locations and represents the combination of the algorithm error and the error from head and eye movements by the subject.
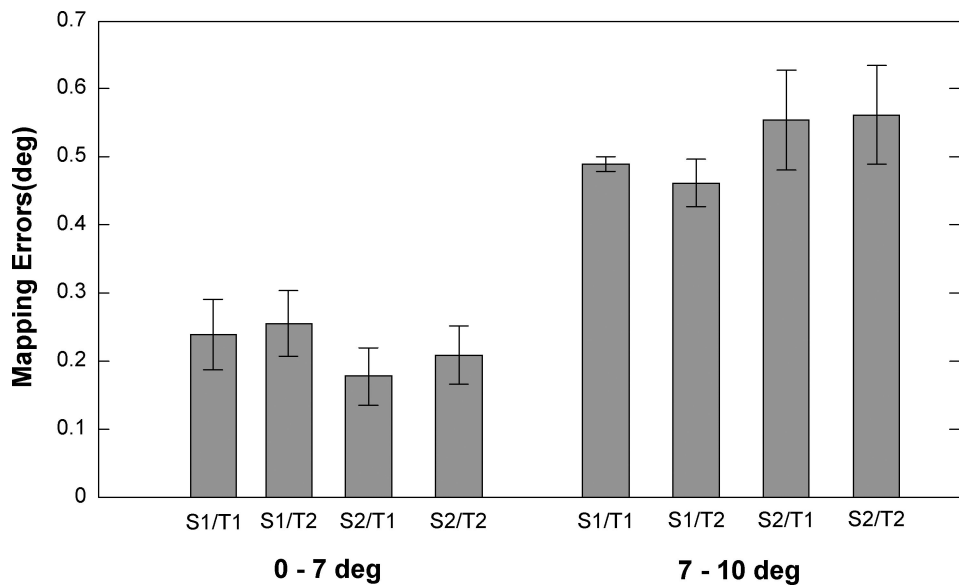
FIGURE 3.

The averaged repeat mapping error measured by imaging multiple locations for subjects 2 and 3 in two different imaging sessions on different days. The error bars represent the standard error for all location within the central ±7° retinal eccentricity (left) or for regions outside the central ±7° (right). S1 = subject1, S2 = subject2, T1 = trial 1, T2 = trial 2. For either subject, two trials were tested at each location on each of 2 days.

than approximately 0.3° or 20% of the frame size (Fig. 3, left) and thus always appeared within the AOSLO image as a recognizable feature. The region outside the central ±7° circular region was also tested, and the averaged mapping error for these more peripheral locations was more than twice as large as for the central region (Fig. 3, right). In the repeatability test, the average mapping error of the second trials on the same subjects were similar to the first trials, as shown in Fig. 3, and no significant difference in accuracy was found ($p > 0.05$) between the two trials.

Imaging using the clinical planning module was efficient in terms of subject time, as shown in Table 1. This time does not include administering informed consent or aligning the subject

to the system. The alignment of the subjects to the AOSLO took approximately 2 min for each subject, although this was variable depending on the need to adjust the patient chair and headrest. The in vivo foveal localization calibration required approximately 1 min once the subject was aligned to the system. For healthy subjects, montages of approximately 13° × 10° required 30 min on average. For two experienced subjects, two extra montages were obtained and the total imaging lasted for about 1 h 15 min. For subject 6 who has the RNFL defect, an approximately 12° × 4.5° montage was acquired in approximately 18 min. We found that the major time-limiting factor was the time required to allow the subject to blink and for AO

TABLE 1.

AOSLO imaging times for acquiring images from each subjects

| Subject list	Montage size	Imaging time (min)
Subject 1	13° × 8.5°	27
Subject 2	13° × 9.4°	35
Subject 3	12.8° × 7.4°	20
Subject 4	Montage 1: 11.8° × 10°	60
	Montage 2: 13° × 10°	
	Montage 3: 7° × 10.5°	
Subject 5	Montage 1: 12° × 8.2°	76
	Montage 2: 6° × 21.7°	
	Montage 3: 8° × 20°	
Subject 6	12° × 4.5°	18

Times only represent the imaging sessions and do not include administering informed consent and aligning the subject to the imaging system. Subjects 1–5 are normal subjects without ocular disease, while subject 6 is a patient with a RNFL defect arising from a cotton wool spot. For subjects 4 and 5, three montages were acquired from each subject, thus the imaging time represents the total elapsed time for all three montages.

to stabilize on the selected retinal layer between locations to maximize image quality.

Montages were successfully built up from the images of all subjects. Fig. 4 shows montages of three large regions of RNFL from subject 5, with the regions indicated by the white boxes on the SLO image from the Heidelberg Spectralis. Nerve fiber bundles can be seen proceeding across the retina from temporal and nasal regions, arcing above and below the fovea and finally approaching the optic disc. At the raphe isolated bundles, interdigitating from the upper and lower retina can also be seen (Fig. 4e). In the videos (not shown) the peripapillary vasculature can be identified due to moving cells within the capillaries. The montage of a region straddling a nerve fiber defect in subject 6 is shown in Fig. 5. Note that the bundle defect appears as a lower contrast and darker region bounded by normal nerve fiber layer near the center of the montage.

DISCUSSION

The mapping approach we developed for the clinical planning module is a generic technique for mapping any standard fundus
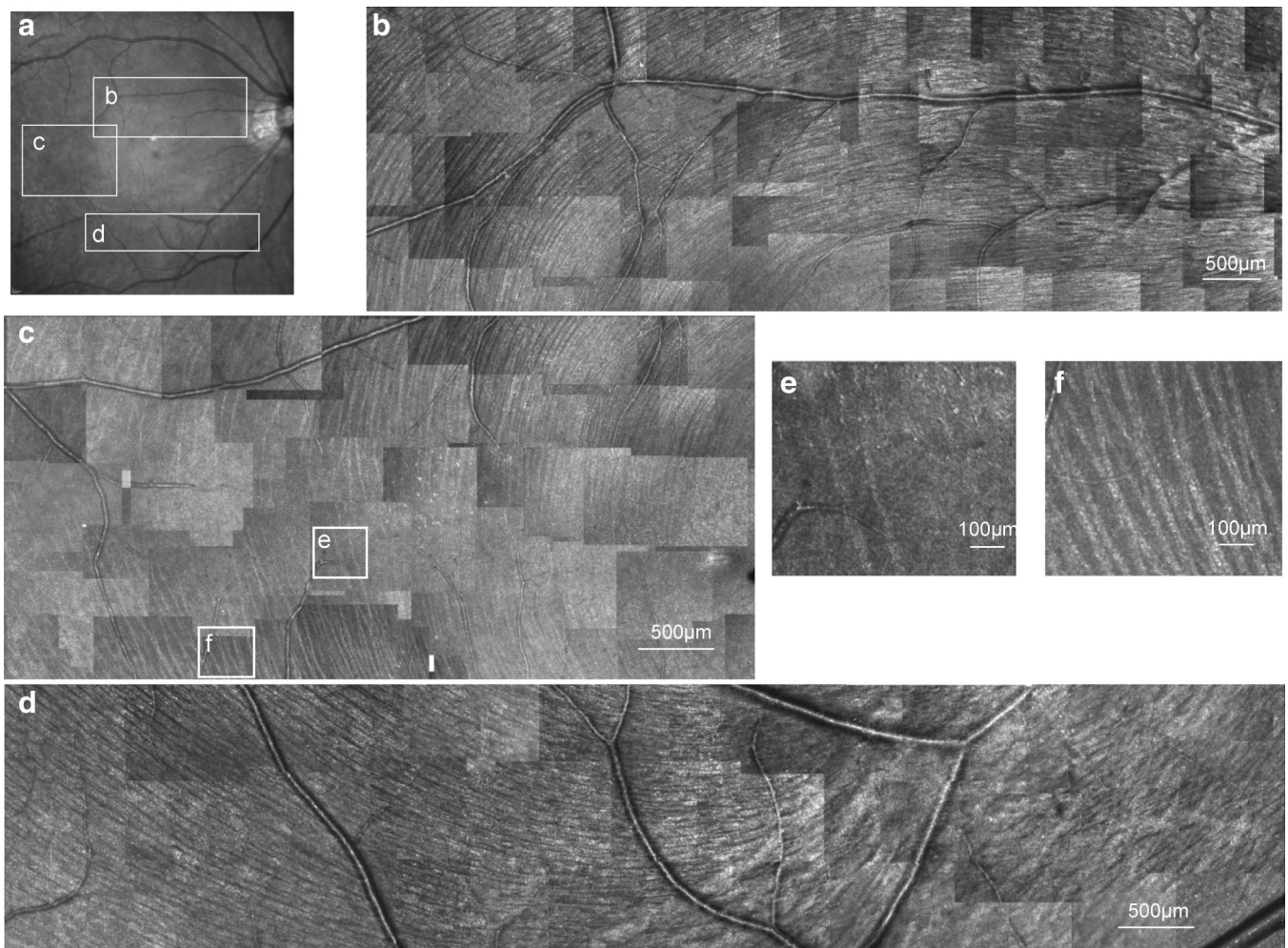
FIGURE 4.

An example of the montage generated using the montage acquisition submodule from subject 5. (a) The SLO fundus image of subject 5. (b–d) Montages constructed from three regions indicated by white squares in (a). Note that while montages (b) and (c) were collected separately with a rest between them, they actually overlap as shown schematically in (a). The white squares in (c) show regions that appear enlarged in (e) and (f).
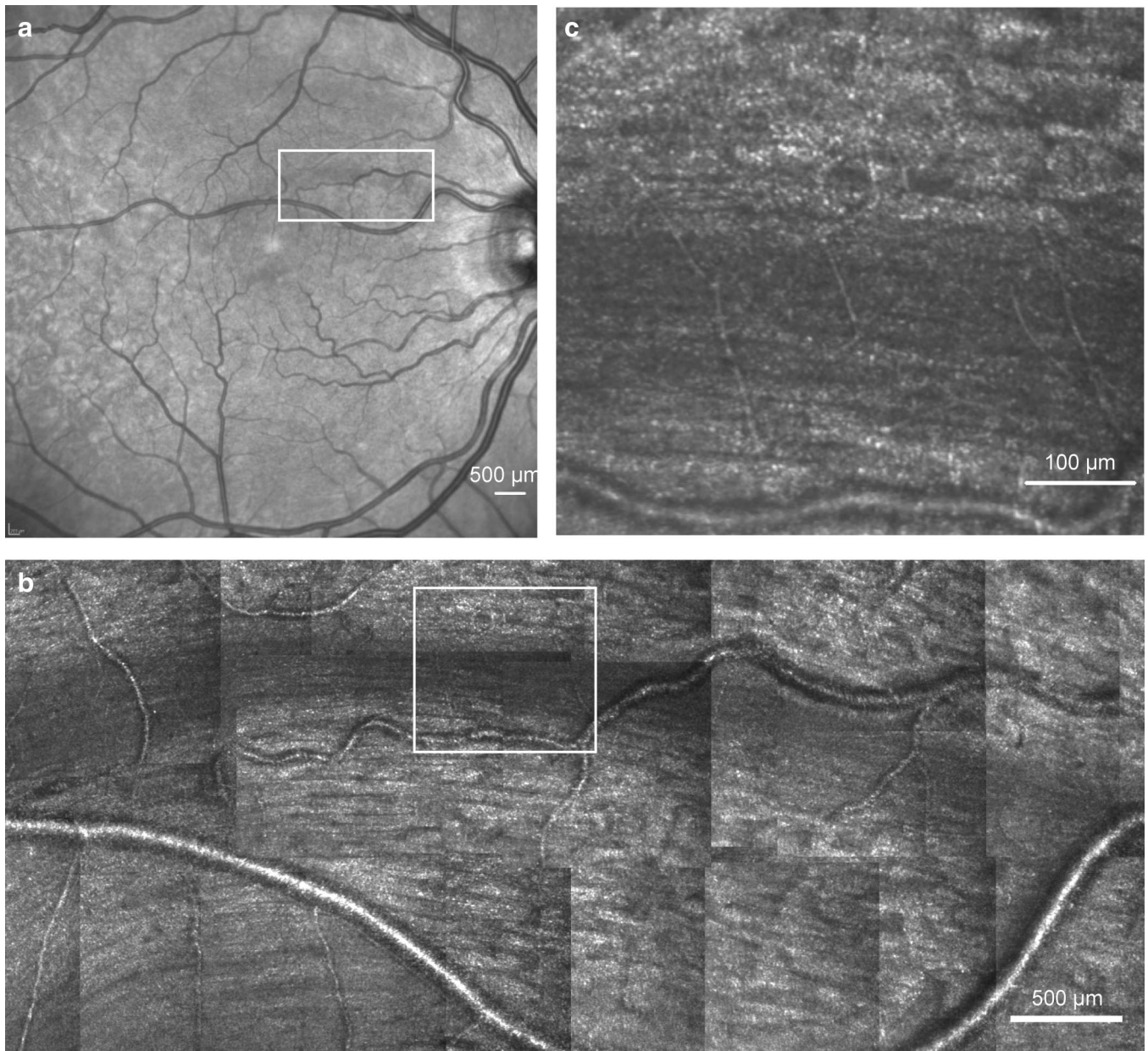
FIGURE 5.

Example of AOSLO imaging of a nerve fiber defect from subject 6. (a) The cSLO image from the Heidelberg Spectralis. The white square in the image schematically indicates the AOSLO imaging region of the RNFL defect. The defect is due to a cotton wool spot and the resulting infarct caused the bundle in the superior nasal quadrant to be damaged. This damaged region can be seen in the SLO image as a dimming of the retinal reflection. (b) The AOSLO montage automatically acquired by clicking within the defect and running a montage file for an approximately 12° × 4.5° region outlined by the white square region in (a). (c) An enlarged view of the section outlined by the white square in (b).

imaging platform to a steerable AOSLO system. The requirement is that the imaging system be constructed according to the telecentric principle. The systems used in this study meet this requirement, as do many other retinal imaging systems.[15] In a telecentric retinal imaging system, the angular pixel position of the retinal images depends only on the visual angle at the pupil of the eye and not on the focus of the system nor the axial length of the eye. This property simplifies the spatial relationship between two telecentric imaging systems allowing us to use a single transformation matrix. As long as the eye being imaged can be assumed not to change significantly between imaging sessions, then the mapping from external angles to internal retinal locations will be similar for a wide-field imaging system and an AOSLO. The mapping itself is required because each imaging platform will have some field distortions and they will not be identical from system to system, rather they depend on the optical design of the particular system. Therefore, the procedures we describe for mapping between the AOSLO and the Spectralis system could be followed for many other fundus imaging systems. However, it is worth noting that there are limitations to the mapping process. First, the mapping matrix itself is not generic for all the systems because each system will have different imaging coordinates, depending on the optical design of the particular system. Second, because the transformation matrix we implemented only incorporates translation, rota-

tion, and scaling, any distortion that changes with field angle, for example, field distortion in the steerable AOSLO, cannot be well modeled by this particular transformation matrix. This is the most likely reason that the transformation matrix performed better toward the center of the field where the field distortion has less impact. Third, as mentioned, we assume that there are not major optical changes in the eye between measurements on the two systems. The most likely optical change that would occur is a change in the accommodative state of the subject. However, we regularly image individuals who are accommodating and we never see major shifts in retinal location with accommodation. The most important limitation is that fixational eye movements are unavoidable.[17] Although stabilization is possible and we have used it,[13] in general it is easier and faster to image a patient without using stabilization. During imaging, a patient may exhibit horizontal, vertical, and torsional eye movements which can occur even within the imaging time for a single frame and cause the images to distort and drift. This places a limit on mapping system accuracy and is the most likely cause for the increased errors we measured in real subjects as opposed to the model eye.

It is important to note that in principle, when mapping, it is possible to construct a more complex matrix where the coefficients of the transformation change with retinal field angle. We did not deem that the extra complexity was justified over the angles subtended by our current systems, because, based on the testing result, the mapping error within the central ±7° range is <20% of the frame size. In addition, for any intended location, we typically use the montage acquisition module to acquire images from more than a single frame location with the smallest likely target region being about 3° × 3°. For regions outside the central ±7°, we simply move the fixation target to a predetermined eccentric location, placing the region of interest within the central field of the AOSLO and redo the in situ calibration.

The implementation of the clinical planning module also provides the possibility of spatially separating the choice of imaging locations, which could be done in the clinic by clicking on regions of clinical interest, and the high-resolution imaging which is performed in the laboratory. The fundus image, together with a list of the coordinates of the regions of interest, could then be transmitted electronically to the AOSLO site. The planning module then could quickly test the indicated locations by reading them in through the montage acquisition interface. Although we have not implemented this remote capability, the process would be no different from the test we did in this study. Thus, the mapping process we have implemented between the two systems makes the remote communications between the two imaging sites more efficient and has the potential to make high-resolution examinations more efficient in terms of both clinician and patient time.

Our approach can be used for imaging any retinal features. In this study, we have demonstrated results for both photoreceptors and RNFL. We have used the RNFL data to reveal a number of structural features of the RNFL. For instance, although anatomical studies[18,19] have shown that nerve fiber bundles combine and split apart, it has not often been possible to see this in vivo except for eyes with localized RNFL defects.[20] However, the AOSLO images show this quite clearly, especially near the raphe where the bundles are relatively sparse in normal eyes. One example is shown in Fig. 4f. Here, the fiber bundles appear non-parallel to each other and

even cross. We also saw that bundles separated and recombined as they crossed blood vessels (not shown) as documented by Zhang et al.[21] Finally, we saw that this indeterminancy of the location of the fiber bundles also occurred along the raphe. In this region, the reflectivity of the retina is relatively weak compared with regions where the RNFL is thicker. This darker appearance is expected based on the high reflectivity over an extended depth that can be seen on OCT imaging near the optic nerve.[22] However, near the raphe, the darker background actually allows very high contrast for the sparse bundles that are present, as shown in Fig. 4e. Because of this, we were able to reliably image bundles down to approximately 4 μm in size. In two of those subjects (subjects 4 and 5), it can be occasionally observed that the bundles projecting across the superior and inferior retina were interdigitated, which indicates that the raphe may not represent a sharp horizontal boundary between the upper and lower visual fields on these two subjects.[23] Ganglion cells in this region could be sending axons along either direction.

The montage acquired from the region of the bundle defect matches the expectation from the arcuate scotoma, typically found to occur with glaucoma and cotton wool spots,[16] and interestingly it is clear that despite the deep scotoma previously documented in this subject,[16] there are some features still oriented within the bundle defect that appear similar to nerve fiber bundles, as shown in Fig. 5b and c. It is not clear whether these are glial or surviving bundles, but their presence is consistent with OCT images of this region where the RNFL layer is thinner, but some tissue remains.[16,24] A similar result is also found in severe glaucoma where the RNFL thickness does not go to zero even when the eye is essentially blind.[25] In addition, although the density of fiber bundles is greatly reduced, it is still possible to see a capillary network crossing the defect and with a higher contrast due to the decreased scattered light from fiber bundles as shown in Fig. 5c. The video recordings (not shown) reveal that the capillaries are functional with blood flow within them.

Overall, the high-resolution images and montages confirm the expected RNFL anatomy. While the larger maps, such as those presented in Fig. 4, still require imaging sessions of an hour or more, and therefore are not desirable for many clinic patients, they can provide insights into the basic properties of the retina and are realistic to perform in normal subjects or motivated research patients using the clinical planning module. For clinical patients, the clinical planning module allows the constructions of montages of about 15° × 10°. This size is realistic for research studies on patients and may provide an alternative way of elucidating structural changes associated with eye diseases as well as monitoring of disease progression. While testing subjects with very poor fixation stability will increase the time for testing, approaches to minimize the impact of eye movements are a topic of active research.[13,26]

CONCLUSIONS

We have implemented a clinical planning module to accurately guide the AOSLO imaging beam to desired locations and to quickly acquire high-resolution AOSLO montages of different sizes. The approach is not only friendly for patients and clinicians but also convenient to relate imaging results across different imaging platforms.

ACKNOWLEDGMENTS

REFERENCES

1. Chui TY, Song H, Burns SA. Individual variations in human cone photoreceptor packing density. J Opt Soc Am (A) 2008;25:3021–9.
2. Song H, Chui TY, Zhong Z, Elsner AE, Burns SA. Variation of cone photoreceptor packing density with retinal eccentricity and age. Invest Ophthalmol Vis Sci 2011;52:7376–84.
3. Dubra A, Sulai Y, Norris JL, Cooper RF, Dubis AM, Williams DR, Carroll J. Noninvasive imaging of the human rod photoreceptor mosaic using a confocal adaptive optics scanning ophthalmoscope. Biomed Opt Express 2011;2:1864–76.
4. Merino D, Duncan JL, Tiruveedhula P, Roorda A. Observation of cone and rod photoreceptors in normal subjects and patients using a new generation adaptive optics scanning laser ophthalmoscope. Biomed Opt Express 2011;2:2189–201.
5. Martin JA, Roorda A. Direct and noninvasive assessment of parafoveal capillary leukocyte velocity. Ophthalmology 2005;112:2219–24.
6. Zhong Z, Petrig BL, Qi X, Burns SA. In vivo measurement of erythrocyte velocity and retinal blood flow using adaptive optics scanning laser ophthalmoscopy. Opt Express 2008;16:12746–56.
7. Tam J, Dhamdhere KP, Tiruveedhula P, Manzanera S, Barez S, Bearse MA, Jr., Adams AJ, Roorda A. Disruption of the retinal parafoveal capillary network in type 2 diabetes before the onset of diabetic retinopathy. Invest Ophthalmol Vis Sci 2011;52:9257–66.
8. Chui TY, Zhong Z, Song H, Burns SA. Foveal avascular zone and its relationship to foveal pit shape. Optom Vis Sci 2012;89:602–10.
9. Morgan JI, Dubra A, Wolfe R, Merigan WH, Williams DR. In vivo autofluorescence imaging of the human and macaque retinal pigment epithelial cell mosaic. Invest Ophthalmol Vis Sci 2009;50:1350–9.
10. Roorda A, Zhang Y, Duncan JL. High-resolution in vivo imaging of the RPE mosaic in eyes with retinal disease. Invest Ophthalmol Vis Sci 2007;48:2297–303.
11. Bedggood P, Daaboul M, Ashman R, Smith G, Metha A. Characteristics of the human isoplanatic patch and implications for adaptive optics retinal imaging. J Biomed Opt 2008;13:024008.
12. Burns SA, Tumbar R, Elsner AE, Ferguson D, Hammer DX. Large-field-of-view, modular, stabilized, adaptive-optics-based scanning laser ophthalmoscope. J Opt Soc Am (A) 2007;24:1313–26.
13. Ferguson RD, Zhong Z, Hammer DX, Mujat M, Patel AH, Deng C, Zou W, Burns SA. Adaptive optics scanning laser ophthalmoscope with integrated wide-field retinal imaging and tracking. J Opt Soc Am (A) 2010;27:A265–77.
14. Zou W, Qi X, Burns SA. Woofer-tweeter adaptive optics scanning laser ophthalmoscopic imaging based on Lagrange-multiplier damped least-squares algorithm. Biomed Opt Express 2011;2:1986–2004.
15. Rudnicka AR, Burk RO, Edgar DF, Fitzke FW. Magnification characteristics of fundus imaging systems. Ophthalmology 1998;105:2186–92.
16. Chui TY, Thibos LN, Bradley A, Burns SA. The mechanisms of vision loss associated with a cotton wool spot. Vision Res 2009;49:2826–34.
17. Stevenson SB, Roorda A. Correcting for miniature eye movements in high resolution scanning laser ophthalmoscopy. In: Manns F, Söderberg P, Ho A, Stuck BE, Belkin M, eds. Ophthalmic Technologies XV: Proceedings of SPIE, Vol. 5688. Bellingham, WA: SPIE Press; 2005:145–51.
18. Henkind P, Levitzky M. Angioarchitecture of the optic nerve. I. The papilla. Am J Ophthalmol 1969;68:979–86.
19. Radius RL, Anderson DR. The histology of retinal nerve fiber layer bundles and bundle defects. Arch Ophthalmol 1979;97:948–50.
20. Jeoung JW, Kim TW, Kang KB, Lee JJ, Park KH, Kim DM. Overlapping of retinal nerve fibers in the horizontal plane. Invest Ophthalmol Vis Sci 2008;49:1753–7.
21. Zhang X, Mitchell C, Wen R, Laties AM. Nerve fiber layer splaying at vascular crossings. Invest Ophthalmol Vis Sci 2002;43:2063–6.
22. Guedes V, Schuman JS, Hertzmark E, Wollstein G, Correnti A, Mancini R, Lederer D, Voskanian S, Velazquez L, Pakter HM, Pedut-Kloizman T, Fujimoto JG, Mattox C. Optical coherence tomography measurement of macular and nerve fiber layer thickness in normal and glaucomatous human eyes. Ophthalmology 2003;110:177–89.
23. FitzGibbon T. The human fetal retinal nerve fiber layer and optic nerve head: a DiI and DiA tracing study. Vis Neurosci 1997;14:433–47.
24. Kocaoglu OP, Cense B, Jonnal RS, Wang Q, Lee S, Gao W, Miller DT. Imaging retinal nerve fiber bundles using optical coherence tomography with adaptive optics. Vision Res 2011;51:1835–44.
25. Sakamoto A, Hangai M, Nukada M, Nakanishi H, Mori S, Kotera Y, Inoue R, Yoshimura N. Three-dimensional imaging of the macular retinal nerve fiber layer in glaucoma with spectral-domain optical coherence tomography. Invest Ophthalmol Vis Sci 2010;51:5062–70.
26. Vogel CR, Arathorn DW, Roorda A, Parker A. Retinal motion estimation in adaptive optics scanning laser ophthalmoscopy. Opt Express 2006;14:487–97.

Gang Huang
Indiana University
School of Optometry
800 East Atwater Avenue
Bloomington, IN 47405
e-mail: gghuang@indiana.edu